Discrete-Time Frequency-Domain Disturbance Observer to Mitigate Harmonic Current in PMSM Drives and the Implementation With Reduced Delay

Mingjin Hu, *Student Member, IEEE*, Wei Hua, *Senior Member, IEEE*, Chenwen Cheng, *Member, IEEE*, Yuchen Wang, and Chunyu Lu

***Abstract*—The disturbance observer (DOB) can be employed in electric drives to improve disturbance rejection. The *Q*-filter of classical frequency-domain DOBs to attenuate multiple harmonic disturbances is high order and faces issues, including discretization, numerical precision, and frequency adaption; thus, its realization in variable-speed drives would be challengeable. This article proposes a discrete-time multifrequency DOB (MFDOB) to address these issues. The *Q*-filter of the proposed design is constructed with an integrator and several parallel resonators in a closed-loop structure. It uses a single parameter per harmonic to control the disturbance rejection bandwidth and the performance is guaranteed under various fundamental frequencies. The impact of the computation delay on the MFDOB-based current control is studied, and the system with less computation delay exhibits a higher stability margin and a wider range of low sensitivity. To eliminate the computation delay, a real-time pulsewidth-modulation update scheme is also developed for the DOB-based two-degree-of-freedom controller. The proposed method is evaluated on a laboratory permanent magnet synchronous machine platform.**

***Index Terms*—Discrete-time, disturbance observer (DOB), harmonic current, multifrequency, variable-speed.**

I. Introduction

HARMONIC contents in ac drives increase system loss, generate torque ripples, and deteriorate power quality. Due to the finite control bandwidth, a single proportional–integral (PI) [1] or proportional–resonant (PR) [2] controller for the regulation of fundamental components offers limited attenuation for harmonic disturbance. To further reduce unexpected harmonic contents in electric drives, various control techniques have been proposed, including resonant control [3], [4], [5], [6], repetitive control [7], [8], disturbance observer (DOB) [9], [10], [11], [12], [13], [14], and iterative learning control. These methods explicitly or implicitly utilize the internal model of harmonic disturbance and realize nearly zero steady-state error at desired harmonic frequencies.

Since the regulation of fundamental components is a primary task, adding the functionality of harmonic suppression should disturb the original control performance as little as possible. The DOB-based schemes provide such an opportunity that the disturbance rejection can be configured separately from the reference tracking in a two-degrees-of-freedom (2-DOF) fashion. In classical frequency-domain DOBs, a *Q*-filter is designed to shape the frequency response of disturbance rejection and the guidelines are well-established for constant or slow-varying disturbances [15]. For periodic disturbance, DOB with repetitive nature is developed [8], while its digital realization is challengeable in variable-speed drives due to the varying and fractional delay. The DOBs dedicated to suppressing a single harmonic disturbance are investigated in [9] and [16] for dual three-phase motors, where the sixth-order current harmonic is compensated and a faster convergence speed compared with PR controller is obtained.

The frequency-domain multifrequency DOB (MFDOB) for multiple harmonics is studied recently [11], [12]. The *Q*-filter employed in MFDOB is high order to embed the internal model of all interested frequencies. A systematic design procedure of MFDOB is proposed in [11] to ensure robust stability for a class of plants with bounded parameter error. The design guidelines for MFDOB considering transients decay rate, steady-state error, and phase margin are proposed in [12]. However, these methods are developed in the continuous-time domain, and practical issues, such as discretization and numerical precision, will arise. The loop delay of the plant is also neglected in [11] and [12], which leads to errors in disturbance estimation. In addition, offline computation is required for these methods; therefore, the parameter tuning and the frequency adaption could be difficult in variable-speed drives.

In digital-control electric drives, the digital delay, including computation delay and modulation delay, generally exists and limits control bandwidth, dynamic performance, and stability margin. The delay constrains the design of the conventional DOBs that the observer bandwidth should be limited to obtain good robustness [17]. Similar limitations also occur in [12] when

Manuscript received 28 November 2022; revised 7 March 2023; accepted 22 April 2023. Date of publication 1 May 2023; date of current version 21 June 2023. This work was supported in part by Key R&D Program under Grant 2021YFB2500701 and in part by Jiangsu Carbon Peak Carbon Neutralization Science and Technology Innovation Special Fund under Grant BE2022032-1. Recommended for publication by Associate Editor H. Hofmann. *(Corresponding author: Wei Hua.)*

The authors are with the School of Electrical Engineering, Southeast University, Nanjing 210096, China (e-mail: hmj@seu.edu.cn; huawei1978@seu.edu.cn; chenwen_cheng@seu.edu.cn; wangyuchen1994@seu.edu.cn; 220202873@seu.edu.cn).

Color versions of one or more figures in this article are available at https://doi.org/10.1109/TPEL.2023.3271651.

Digital Object Identifier 10.1109/TPEL.2023.3271651

designing MFDOB. Regarding the discrete-time system, the relative order of the plant has a similar effect as the time delay. For the motion control system, Sariyildiz et al. [18] show that the design constraints on discrete-time DOB can be lessened if the acceleration measurement is used instead of velocity or position measurement, as the former reduces the phase lag in feedback and enables a lower relative order of the controlled plant.

To reduce the digital delay in ac drives, multisampling techniques [19] or real-time updating schemes by shifting the sampling instant toward the pulsewidth-modulation (PWM) command update instant [20] can be employed, while they are susceptible to aliasing due to asynchronous sampling process. Alternatively, the PWM command can be updated immediately after it is computed, which keeps the synchronous sampling and avoids the aliasing [21], [22]. However, the computation time should be very short to alleviate the degradation in dc bus voltage utilization. A method for linear 1-DOF controllers to minimize update latency is developed in [21], but it is not suitable for 2-DOF controllers, including the DOB-based controller. Considering the computation load increases with the controlled harmonics, the implementation of MFDOB with real-time updating would be challenging.

This article proposes a discrete-time MFDOB for harmonic current reduction in permanent magnet synchronous machine (PMSM) drives. It allows variable-frequency operation and avoids the discretization and frequency adaption issues of MFDOB designed in the continuous-time domain [11], [12]. The proposed MFDOB uses a single parameter per harmonic to determine the suppression bandwidth and there is a guaranteed stability margin for various fundamental frequencies. To implement the proposed MFDOB with zero computation delay, a real-time calculation scheme is developed with minimized update latency and can be extended to other 2-DOB controllers. The rest of this article is organized as follows. Section II introduces the preliminaries. The proposed MFDOB is presented in Section III and the controller synthesis is given in Section IV. The real-time implementation of MFDOB with reduced digital delay is developed in Section V. The experimental results are presented in Section VI to validate the proposed method. Finally, Section VII concludes this article.

II. Preliminaries

A. Model of PMSM Drives

In the synchronous *dq* axes frame, the voltage equation of a nonsalient PMSM in complex-vector form is

$$u_{dq} = R_s i_{dq} + L_s \frac{d}{dt} i_{dq} + j\omega_e L_s i_{dq} + j\omega_e \psi_{mdq} \tag{1}$$

where $j = \sqrt{-1}$ is the imaginary unit, $i_{dq} = i_d + j \cdot i_q, u_{dq} = u_d + j \cdot u_q$, and $\psi_{mdq} = \psi_{md} + j \cdot \psi_{mq}$ are the complex vectors of *dq* axes current, voltage, and permanent magnet (PM) flux, respectively, ω_e is the fundamental frequency, and R_s and L_s are the resistance and inductance of stator winding, respectively.

Based on (1), the complex transfer function from u_{dq} to i_{dq} is obtained as (2) with s being the Laplace operator

$$P_{RL}(s) = \frac{1}{R_s + sL_s + j\omega_e L_s}. \tag{2}$$

If any nonlinear effects of the PWM are disregarded, the output voltage is considered to be piecewise constant in the stationary reference frame and modeled by a zero-order hold (ZOH) element. The ZOH together with the sampler gives $G_{\text{PWM}}(s) = \frac{1-e^{-sT_s}}{sT_s}$, where T_s is the sampling period. Often the PWM is simplified to $G_{\text{PWM}}(s) \approx e^{-0.5sT_s}$. In addition, to provide sufficient time for analog-to-digital conversion and digital computation, the PWM reference is delayed by the computation time T_c to update, which can be modeled by a pure delay of the form $G_d(s) = e^{-sT_c}$. Typical value of T_c is $1T_s$. Therefore, a total time delay of $T_d = 0.5T_s + T_c$ exists in the current control.

By transforming $G_{\text{PWM}}(s)$ and $G_d(s)$ to the *dq* axes frame with the frequency-shift property, the plant of the current control is obtained as follows:

$$\begin{aligned} P(s) &= P_{RL}(s)\, G_{\text{PWM}}(s + j\omega_e)\, G_d(s + j\omega_e) \\ &\approx \frac{e^{-j\omega_e T_d} e^{-sT_d}}{R_s + sL_s + j\omega_e L_s}. \end{aligned} \tag{3}$$

B. Harmonic Disturbance of Current Control

The harmonic disturbance in the current control of PMSM can come from various aspects as follows [6], [23].

1) Flux Harmonics: The magnetic field of the PM is usually assumed to have an ideal sinusoidal distribution in space. However, due to stator slotting, magnetic saturation, and manufacturing issues, the PM flux is possible to contain space harmonics, giving

$$\begin{cases} \psi_{md} = \psi_{md,0} + \sum_{k=1}^{\infty} \psi_{md,k} \cos(6k\theta) \\ \psi_{mq} = \sum_{k=1}^{\infty} \psi_{mq,k} \cos(6k\theta) \end{cases} \tag{4}$$

where $\theta = \int \omega_e t$ is the rotor electrical angle, $\psi_{md,0}$ is the dc component of the *d*-axis flux, and $\psi_{md,k}$ and $\psi_{mq,k}$ are the amplitudes of the six *k*th flux harmonic of the *d*- and *q*-axis, respectively. According to (1), time harmonics of voltage disturbance are induced by the term $j\omega_e \psi_{mdq}$.

2) Stator Winding Asymmetry: The asymmetry of stator winding causes negative sequence in phase current, which is the second-order harmonic when seen from the *dq* axes frame.

3) Deadtime Effect: The voltage distortion induced from the deadtime effect of the inverter can be expressed by (5), which is also the combination of six *k*th harmonics in *dq* axes

$$\Delta u_{dq} = \Delta U \left[-1j + \sum_{k=1}^{\infty} \frac{12k \sin(6k\omega_e t) + j2\cos(6k\omega_e t)}{36k^2 - 1} \right] \tag{5}$$

where ΔU is a constant depending on the hardware.

The above-mentioned periodic disturbance, together with aperiodic disturbance, including uncompensated back electromotive force and parameter uncertainty, can be represented by a lumped disturbance d in the input channel, and the current

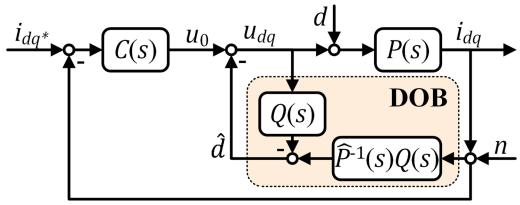

Fig. 1. Closed-loop system with the DOB structure (shaded block).

control system is given by

$$i_{dq}(s) = P(s)\left(u_{dq}(s) + d(s)\right). \tag{6}$$

C. Structure of DOB-Based Control System

Fig. 1 shows the control system with a DOB, where $\hat{P}(s)$ is a minimum-phase nominal model with a relative order p, $C(s)$ is the outer-loop controller, u_0 is the output of $C(s)$, $Q(s)$ is known as the "Q-filter" to reject the disturbance d. In the frequency range of $Q(j\omega) \approx 1$, the system has the response [15]

$$\begin{aligned} i_{dq} &= \Psi^{-1}(s)\,\hat{P}(s)\left(u_0 + (1 - Q(s))\,d + Q(s)\,n\right) \\ &\approx \hat{P}(s)\,u_0 + \hat{P}(s)\,(1 - Q(s))\,d + \hat{P}(s)\,Q(s)\,n \end{aligned} \tag{7}$$

where $\Psi(s) = P^{-1}(s)\hat{P}(s)(1 - Q(s)) + Q(s)$.

Based on the analysis in the Section II-B, the disturbance d with the following form is considered:

$$d(t) = A_0 + \sum_{k=1}^{n} A_k \cos\left(h_k \omega_e t + \varphi_k\right) \tag{8}$$

where $n \geq 1$, h_k is a known harmonic order, A_k and φ_k are the unknown constants, and ω_e is the fundamental frequency, which is available from a position sensor or phase-locked loop.

In [11] and [12], the Q-filter for multiple harmonic disturbance elimination is formulated in a high-order rational fraction, such as

$$Q(s) = \frac{\sum_{k=0}^{N} \beta_k s^k}{\sum_{k=0}^{M} \alpha_k s^k}. \tag{9}$$

Laplace transform of the disturbance $d(t)$ has the form of $d(s) = A_0/s + \sum_{k=1}^{n}(\bar{\sigma}_k s + \tilde{\sigma}_k)/(s^2 + h_k^2\omega_e^2)$, where $\bar{\sigma}_k$ and$\tilde{\sigma}_k$ are some constants. If the numerator of $S_Q(s) \triangleq 1 - Q(s)$ contains $s\prod_{k=1}^{n}(s^2 + h_k^2\omega_e^2)$, then the response $y(t)$ will completely reject the disturbance $d(t)$ at steady state. Similarly, for a discrete-time Q-filter, $Q(z)$, the numerator of $S_Q(z) \triangleq 1 - Q(z)$ should contain $(z-1)\prod_{k=1}^{n}(z^2 - 2z\cos h_k\omega_e T_s + 1)$ to realize robust disturbance rejection performance (where T_s is the sampling period). In this manner, the coefficients of such a Q-filter are functions of the fundamental frequency ω_e.

The implementation of (9) could be problematic for variable-speed drives considering the following issues.

1) The discretization of $Q(s)$ should preserve the frequency characteristics around the desired harmonic frequencies. The conventional Tustin method with prewarping cannot realize this goal for more than one harmonic. Methods, such as zero–pole matching and impulse invariant, are qualified but there is no trivial solution for the discretized filter.
2) Even $Q(s)$ has been properly discretized and yields a $Q(z)$, it is a high-order filter with a relative order larger than $p + 2n$. Implementing such a high-order discrete-time transfer function will face poor numerical precision [24].
3) Because the coefficients of $Q(z)$ are dependent on the harmonic frequencies and varying with the fundamental frequency in variable-speed drives, the implementation of $Q(z)$ should maintain a simple frequency adaption.

In addition, since $\hat{P}^{-1}(s)Q(s)$ needs to be realized, the delay of the actual plant $P(s)$ is approximated or neglected [12] in the nominal plant $\hat{P}(s)$, which leads to modeling error and degrades the stability. The above issue will be addressed in Section III with a direct discrete-time design.

D. Constraint of Time Delay

The time delay constrains the design of the conventional DOB-based control systems [17] and it will be shown that such constraints are similar in multifrequency control systems. The open-loop transfer function in the form of $L(s) = L_0(s)e^{-T_d s}$ is considered, where $L_0(s)$ is the minimum phase and strictly proper. According to the Bode integral theorem, the sensitivity function satisfies

$$\int_0^\infty \ln|S(j\omega)|\,d\omega = 0. \tag{10}$$

Equation (10) reflects the waterbed effect that pushing sensitivity down at one point will result in an increased level somewhere. Considering a design specification in the form of (11) when multiple harmonic disturbances are to be rejected

$$|S(j\omega)| \leq \alpha < 1\ \forall\omega \in \Theta_k, k = 0, 1, \ldots, n \tag{11}$$

where $\Theta_k \triangleq (h_k\omega_e - 0.5\beta_k, h_k\omega_e + 0.5\beta_k)$ for $k = 1, \ldots, n$ and $\Theta_0 \triangleq [0, \beta_0)$ are predefined ranges that require small sensitivities. According to (10), increasing β_k for higher control bandwidth must come at the expense of a larger peak in $|S(j\omega)|$. The limitation may not be so strict as the increase in area can come over an infinite frequency range. However, the time delay imposes another constraint on the sensitivity function as described by [25]

$$\left|\int_{R_\delta}^\infty \ln|S(j\omega)|\,d\omega\right| \leq \frac{3\pi\delta}{2T_d} \tag{12}$$

where $\delta < 0.5$ and R_δ, l are some constants so that $|L_0(s)| \leq \delta(R_\delta/|s|)^l\ \forall s \in \Omega(R_\delta) \triangleq \{s : \mathrm{Re}[s] \geq 0 \text{ and } |s| \geq R_\delta\}$ [25]. The selection of R_δ can refer to the articles presented in [17] and [25] for more details and generally a larger open-loop gain results in a large δ. Equation (12) shows that the integration of the tail of the sensitivity function is limited when time delay exists.

For the sake of simplicity, we assume that Θ_0, Θ_1,…, Θ_n and $[R_\delta, \infty)$ are mutually exclusive. Then, based on (10)–(12), the lower bound of the sensitivity function can be deduced as

follows:

$$M_s \triangleq \sup_{\omega} |S(j\omega)| \geq \exp\left(\frac{\sum_{k=0}^{n} \beta_k \ln \frac{1}{\alpha} - \frac{3\pi\delta}{2T_d}}{R_\delta - \sum_{k=0}^{n} \beta_k}\right). \quad (13)$$

Since the sensitivity function represents the inverse of the distance of the open-loop transfer function to the critical point $(-1, 0j)$ at each frequency ω in the Nyquist diagram, the sensitivity peak M_s is a compact indicator of stability. Equation (13) reveals that a large delay T_d and high control bandwidth (lower β_k or α) will amplify the sensitivity peak and consequently degrade the stability margin. It suggests that the cumulated bandwidth should be limited when the fundamental component and multiple harmonic components are regulated. Reducing the time delay could relieve such constraints.

III. Discrete-Time Frequency-Domain MFDOB

A. Structure

To avoid the defects of discretizing an s-domain Q-filter, this section proposes a direct design in the z-domain. For the computation delay T_c being multiple of T_s, the plant dynamics seen from the digital controller is

$$P(z) = \frac{b}{z^{p-1}(z-a)} \quad (14)$$

where $a = e^{-(R_s/L_s + j\omega_e)\cdot T_s}$, $b = (1-a)e^{-jp\omega_e T_s}/R_s$, and $p = T_c/T_s + 1$ is the relative order. We also denote $\hat{P}(z)$ as the nominal model for $P(z)$. The fractional-order computation delay is not considered in this article as it will lead to a plant zero with negative real part [26].

To realize the robust rejection of disturbance at the specific frequencies, the Q-filter is constructed as follows:

$$Q(z) = \frac{L_Q(z)}{1 + L_Q(z)} \quad (15)$$

$$L_Q(z) = G_f(z)\left(\frac{l_0}{z-1} + \sum_{k=1}^{n} \frac{z l_{2k-1} + l_{2k}}{z^2 - 2c_k z + 1}\right) \quad (16)$$

where $G_f(z)$ is a filter to shape the loop gain $L_Q(z)$, $l_0, \ldots, l_{2n}$ are the undetermined parameters, and $c_k = \cos h_k \omega_e T_s$. The high-order filter $Q(z)$ is decomposed with an integrator and several resonators in a closed-loop architecture to ease digital realization. The infinite gains of $L_Q(z)$ at the resonant frequencies ensure the complete disturbance rejection for target harmonics with $Q(z)$, i.e., $Q(e^{jh_k\omega_e T_s}) = 1$.

The estimated disturbance with a frequency-domain DOB is $\hat{d} = Q(z)\hat{P}^{-1}(z) i_{dq} - Q(z) u_{dq}$. To avoid realizing $Q(z)$ twice, $\hat{d}$ is reformulated using (15) and yields

$$\begin{aligned}\hat{d} &= L_Q(z)\left[\hat{P}^{-1}(z) i_{dq} - u_{dq} - \hat{d}\right] \\ &= z^p L_Q(z)\left[z^{-p}\hat{P}^{-1}(z) i_{dq} - z^{1-p}\left(z^{-1}u_{dq} + z^{-1}\hat{d}\right)\right].\end{aligned} \quad (17)$$

Based on (16) and (17), the proposed MFDOB is constructed, as shown in Fig. 2. In Fig. 2(a), an explicit delay in the blue area is arranged to avoid algebraic-ring issues in realization. The saturated voltage $\bar{u}_{dq}$ is fed to MFDOB to maintain the consistency with the actual plant. In linear analysis, the saturation block "Sat." is regarded as a unity gain and $\bar{u}_{dq} = u_{dq}$ is assumed. If $\hat{P}(z)$ is accurate, the inner-loop sensitivity and complementary sensitivity are $S_i(z) = S_Q(z) \triangleq 1 - Q(z)$ and $T_i(z) = Q(z)$, respectively.

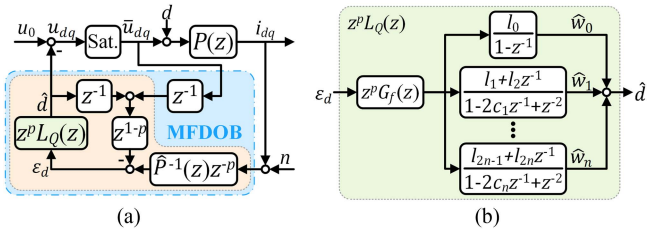

Fig. 2. (a) Structure of the proposed MFDOB. (b) Implementation of $z^p L_Q(z)$.

To reduce the underdetermined design parameters, the minimal realization of $G_f(z)$ is considered, giving

$$G_f(z) = 1/\left(z^{p-1} + \alpha_{p-2} z^{p-2} + \ldots + \alpha_0\right) \quad (18)$$

where $\alpha_0, \ldots, \alpha_{p-2}$ are the coefficients ($\alpha_0 = 1$ if $p = 1$).

The frequency response of the $Q(z)$ dominates the performance of the inner-loop disturbance rejection. The value of $Q(e^{j\omega T_s})$ close to 1 indicates the accurate estimation and effective attenuation of the disturbance at frequency ω, which has two requirements: the magnitude $|Q(e^{j\omega T_s})|$ is near 1 and its phase is near zero. The magnitude of the sensitivity function $S_Q(z) = 1 - Q(z)$ is a more compact indicator since the $Q(z)$ close to 1 always lead to a low $|S_Q(z)|$. Therefore, in this article, we design the sensitivity function to have the following form:

$$S_Q(z) = \frac{1}{1 + L_Q(z)} = \frac{(z-1) D_f(z)}{(z-1+\lambda)^p} \prod_{k=1}^{n} \frac{\Phi_k^{ol}(z)}{\Phi_k^{cl}(z)} \quad (19)$$

where $\Phi_k^{cl}(z) = \Phi_k^{ol}(z) + 2\rho_k(c_k z - 1)$, $\Phi_k^{ol}(z) = z^2 - 2c_k z + 1$, λ and ρ_k are the design parameters to adjust the bandwidth for aperiodic disturbance and the kth harmonic component ($k = 1, \ldots, n$), respectively, and $\lambda, \rho_k \in [0, 1]$.

Fig. 3(a) shows the frequency response of $\Phi_k^{ol}(z)/\Phi_k^{cl}(z)$, which is a notch filter around the harmonic frequency. Its gain in passband is $(1 - \rho_k)^{-1}$ and the notch width is approximately defined by ρ_k/T_s. The term $\Phi_k^{ol}(z)/\Phi_k^{cl}(z)$ determines the shape of $S_Q(z)$ around the harmonic frequency $h_k\omega_e$. The root loci of $\Phi_k^{cl}(z)$ and $\Phi_k^{cl}(z)$ with the harmonic frequency increasing are shown in Fig. 3(b).

The relative order implies the time delay of the control loop. Hence, the discrete-time system will face similar restrictions as the case in the continuous-time domain [see (13)].

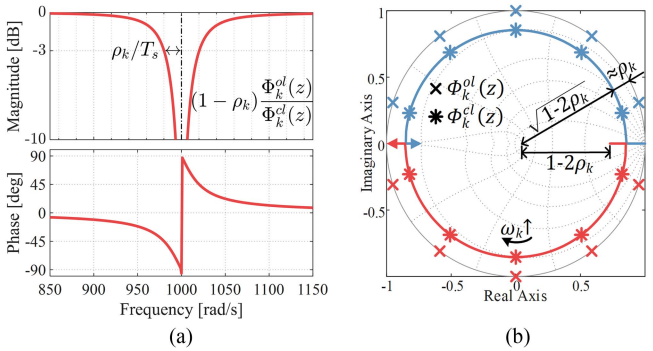

Fig. 3. (a) Frequency response of $\Phi_k^{ol}(z)/\Phi_k^{cl}(z)$. (b) Diagrammatic loci of roots of Φ_k^{ol} and $\Phi_k^{cl}(z)$ with $h_k\omega_e$ being $0 \to \pi/T_s$.

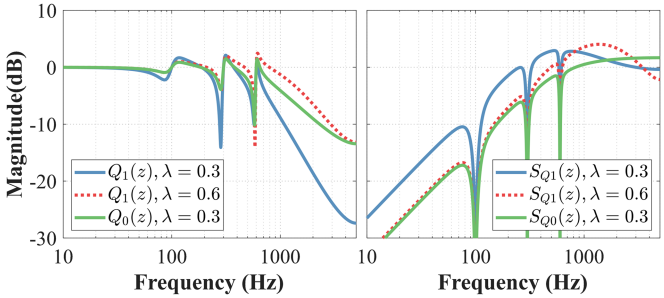

Fig. 4. Magnitude of the Q-filter and sensitivity function. The frequencies of the three harmonics are 100 Hz, 300 Hz, and 600 Hz. Conditions: $\rho_1 = \rho_2 = \rho_3 = 0.01$ and $T_s = 100\ \mu$s.

B. Conventional Case: $T_c = T_s$

In this case, the minimal realization of $G_f(z)$ is $G_f(z) = 1/(z+\alpha_0)$ and the sensitivity function is expressed by

$$S_{Q1}(z) = \frac{(z+\alpha_0)(z-1)}{(z-1+\lambda)^2}\prod_{k=1}^{n}\frac{\Phi_k^{ol}(z)}{\Phi_k^{cl}(z)}. \tag{20}$$

The magnitudes of the Q-filter and sensitivity function are shown in Fig. 4. Substituting (16) into (15) and comparing the coefficients of z^{2n+1} of the denominator with $S_Q(z)$ in (20) yields $\alpha_0 = 2\lambda - 1 + 2\sum_{k=1}^{n}\rho_k c_k$. To avoid import unstable open-loop poles, $-1 \le \alpha_0 \le 1$ should be satisfied, yielding $\lambda + \sum_{k=1}^{n}\rho_k c_k \le 1$. The dependence of α_0 on λ and $\sum_{k=1}^{n}\rho_k c_k$ implies that the frequency response of $S_{Q1}(z)$ may not be freely configured. According to Fig. 3(a), it is easy to identify that increasing ρ_k will widen the notch width, while the sensitivity elsewhere will be amplified by $(1-\rho_k)^{-1}$. Increasing λ will also improve the bandwidth of disturbance rejection at low frequencies. However, considering the sensitivity function at $\omega = \pi/T_s$, given by $\gamma \triangleq S_{Q1}(-1) = \frac{4(1-\lambda-\sum_{k=1}^{n}\rho_k c_k)}{(2-\lambda)^2\prod_{k=1}^{n}(1-\rho_k)}$, we have $\gamma \ge 0$ and $\frac{\partial\gamma}{\partial\lambda} = \frac{-4(\lambda+2\sum_{k=1}^{n}\rho_k c_k)}{(2-\lambda)^3\prod_{k=1}^{n}(1-\rho_k)} < 0$. It shows increasing λ will lower the tail of sensitivity function, and under the constraint of Bode integral theorem, the sensitivity peak will be amplified, which is witnessed in the left column of Fig. 4 by comparing $S_{Q1}(z)$ with $\lambda = 0.3$ and $\lambda = 0.6$.

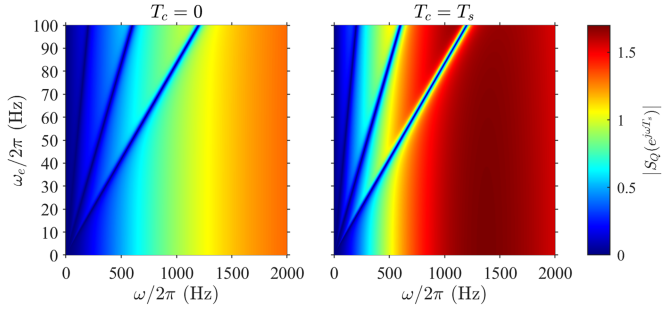

Fig. 5. Plot of $|S_Q(e^{j\omega T_s})|$ as a function of $\omega/2\pi$ and fundamental frequency $\omega_e/2\pi$. Three harmonics with frequencies being $2\omega_e$, $6\omega_e$, and $12\omega_e$ are controlled. Equations (22) and (23) are employed with $\lambda = 0.6$ and $\rho_1 = \rho_2 = \rho_3 = 0.02$.

C. Reduced Digital Delay With $T_c = 0$

If the computation delay is reduced to 0, the plant $P(z)$ has a relative order of 1. Hence, the minimal realization of $G_f(z)$ is $G_f(z) = 1$, and the desired sensitivity function is obtained as follows:

$$S_{Q0}(z) = \frac{z-1}{z-1+\lambda}\prod_{k=1}^{n}\frac{\Phi_k^{ol}(z)}{\Phi_k^{cl}(z)}. \tag{21}$$

Similarly, the sensitivity peak of $S_{Q0}(z)$ is increased with higher λ and ρ_k. However, due to the reduced relative order, $S_{Q0}(z)$ does not have a parameter α_0 analogous to $S_{Q1}(z)$ and, thus, the constraints are lessened. The magnitudes of the Q-filter and sensitivity function are also plotted in Fig. 4 as green lines. The sensitivity peak of $S_{Q0}(z)$ is lower than $S_{Q1}(z)$. In addition, $S_{Q0}(z)$ requires a half λ of $S_{Q1}(z)$ to realize similar disturbance rejection at low frequency. Here, λ/T_s can be considered as an approximate bandwidth of $\frac{z-1}{z-1+\lambda}$, i.e., the first term of $S_{Q0}(z)$. This comparison illustrates the superiority of $S_{Q0}(z)$ over $S_{Q1}(z)$, which has been previewed in Section II-C.

The solution of $l_0, \ldots, l_{2n}$ for both (20) and (21) are getting rather complex as the number of controlled harmonics grows. Approximations of the solutions for (20) and (21) are given in (22) and (23), respectively, which are the extensions of the case $n = 1$ and shows sufficient accuracy when $\sum_{k=1}^{n}\rho_k c_k \ll \lambda$

$$\begin{cases} l_0 \approx \lambda^2\left(1-\sum_{k=0}^{n}\rho_k\right) \\ l_{2k-1} \approx \rho_k\left((2c_k+\lambda)^2 - 2(c_k+1)\right) \\ l_{2k} \approx \rho_k\left(\lambda^2+2-4\lambda-2c_k\right),\ k=1,2,\ldots,n \end{cases} \tag{22}$$

$$\begin{cases} l_0 \approx \lambda\left(1-\sum_{k=0}^{n}\rho_k\right) \\ l_{2k-1} \approx \rho_k(2c_k+\lambda) \\ l_{2k} \approx -\rho_k(2-\lambda),\ k=1,2,\ldots,n. \end{cases} \tag{23}$$

Fig. 5 illustrates the sensitivity functions $S_{Q0}(e^{j\omega T_s})$ and $S_{Q1}(e^{j\omega T_s})$ with the harmonic frequencies synchronized to a sweep of the fundamental frequency. Three blue traces in the two graphs are relevant to the low sensitivity for the three target harmonics. The blue range with small ω indicates the rejection capability to aperiodic disturbance. Fig. 5 shows that the two cases have flat frequency responses for various ω_e, while

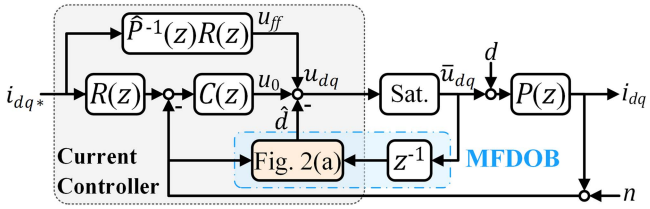

Fig. 6. Block diagram of the proposed MFDOB-based current control.

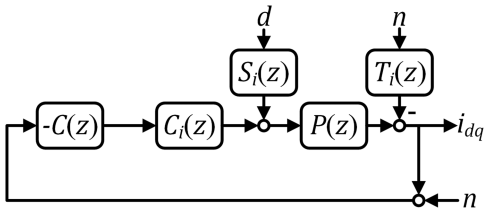

Fig. 7. Equivalent block diagram of the outer-loop feedback control.

$S_{Q0}(z)$ shows an overall lower sensitivity with the reduced delay.

IV. Analysis and Synthesis of the MFDOB

Fig. 6 presents the block diagram of the proposed MFDOB-based current control, where $C(z)$ is the outer-loop controller and $R(z)$ is the reference model. Fig. 7 illustrates the equivalent block diagram of the outer-loop feedback control. The disturbance d is attenuated by $S_i(z)$ before it enters the outer loop. The sensitivity and complementary sensitivity functions of the outer loop can be obtained as follows:

$$S_o(z) = \frac{1}{1+L_o(z)},\ T_o(z) = \frac{L_o(z)}{1+L_o(z)} \tag{24}$$

where $L_o(z) = C(z)C_i(z)P(z)$ and $C_i(z) = \frac{\hat{P}(z)}{Q(z)P(z)+S_Q(z)\hat{P}(z)}$. Since $C_i(z)P(z) \approx \hat{P}(z)$ at the frequencies ω with small inner-loop sensitivity ($S_Q(e^{j\omega T_s}) \approx 0$), the controlled object seen from u_0 can be regarded as the nominal plant $\hat{P}(z)$.

The closed-loop complementary sensitivity function $T(z)$ and the sensitivity function $S(z)$ are deduced as follows:

$$S(z) = S_i(z)\,S_o(z) \tag{25}$$

$$T(z) = S_o(z)\,T_i(z) + T_o(z). \tag{26}$$

Equation (25) shows both the DOB and the outer-loop controller that contribute to the disturbance rejection of the closed-loop system. The functionality of harmonic elimination can be added to either the DOB or the outer-loop controller; however, the advantage of utilizing the proposed MFDOB is that the resonant mode will not be excited by the reference signal in the nominal case.

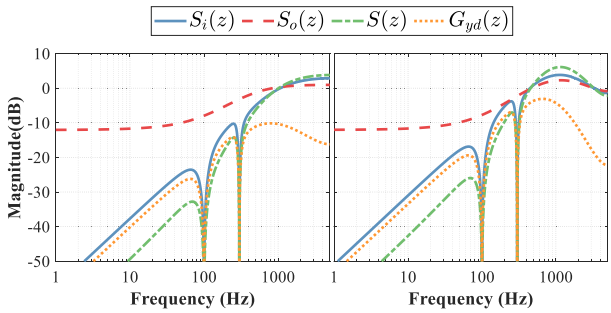

Fig. 8. Frequency responses of the sensitivity functions and the disturbance rejection. The parameters are $\lambda = 0.5$, $\rho_1 = \rho_2 = \rho_3 = 0.02$, $K_p = 1$, $R_s = 0.29\,\Omega$, $L_s = 0.5$ mH, and $f_e = 50$ Hz. (Left column: $T_c = 0$ and Right column $T_c = 1T_s$.)

Considering the saturation block as a unit gain, the equivalent control law can be derived as follows:

$$u_{dq}(z) = \underbrace{R(z)\left(\hat{P}(z)^{-1} + C(z)\right)(1+L_Q(z))}_{K_{ff}(z)} i_{dq*}(z) - \underbrace{\left(C(z) + C(z)L_Q(z) + \hat{P}(z)^{-1}L_Q(z)\right)}_{K_{fb}(z)} i_{dq}(z) \tag{27}$$

where $K_{ff}(z)$ and $K_{fb}(z)$ represent the transfer function from the current reference and feedback to the output voltage, respectively. The two are different due to the 2-DOF structure.

As $L_Q(z)$ includes an integrator and several resonators, $K_{fb}(z)$ can be regarded as a special proportional–integral–resonant controller. Similar equivalence between the DOB-based controller and PI controller has also been revealed in [27].

Various outer-loop controllers can be synthesized with the proposed MFDOB. Noting that if $C(z)$ is a PI-like controller, $S(z)$ will have two zeros at $z = 1$ and the closed-loop system can reject a ramp-type disturbance with zero steady-state error, which is analogous to other control schemes with cascaded DOB to attenuate high-order disturbance [28]. In this article, the aperiodic disturbance of interest is of constant type; thus, the simple proportional control, i.e., $C(z) = K_p$, is sufficient and will be employed in the following analysis.

Fig. 8 shows the sensitivity functions when zero-sample and one-sample computation delay are employed. The closed-loop responses to the exogenous disturbance are also illustrated as the traces of $G_{yd}(z)$. Noting that disturbance rejection response can be expressed by $G_{yd}(z) = S(z)P(z)$, i.e., the sensitivity $S(z)$ also represents how the closed-loop system responds to disturbance compared with the open-loop system. The overall disturbance suppression is determined by $S(z) = S_i(z)S_o(z)$. The robustness against the disturbance is significantly improved as the inner-loop MFDOB rejects the disturbance at desired frequencies, and the outer-loop controller offers additional attenuation at low-frequency ranges.

In Fig. 8, the sensitivity peaks of $S_i(z)$, $S_o(z)$, and $S(z)$ with $T_c = T_s$ are higher than those with $T_c = 0$ due to the limitation

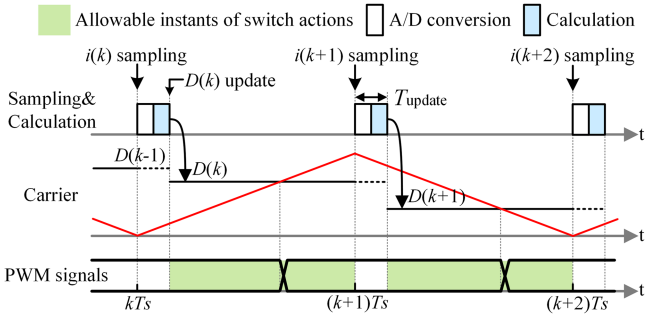

Fig. 9. PWM command $D(k)$ is updated immediately after sampling the current with a latency T_{update}, and it remains active until the next update event, i.e., from kT_s+T_{update} to $(k+1)T_s+T_{\text{update}}$.

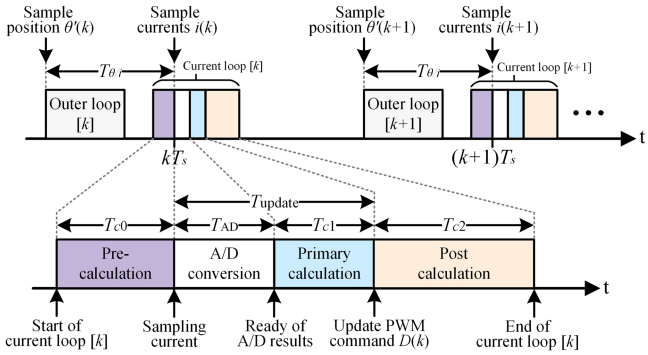

Fig. 10. Schedule for the proposed current control scheme.

caused by time delay, which again illustrates the superiority of employing a reduced digital delay.

The sensitivity peak of $S(z)$ can be evaluated by

$$M_s = \max_{\omega} S\left(e^{j\omega T_s}\right) \leq M_s^i \cdot M_s^o \tag{28}$$

where $M_s^i = \max_{\omega} S_i(e^{j\omega T_s})$ and $M_s^o = \max_{\omega} S_o(e^{j\omega T_s})$ are the sensitivity peaks of the inner loop and the outer loop, respectively. Both M_s^i and M_s^o are bounded with given control parameters for $T_c = T_s$ and $T_c = 0$, and the derivation can be found in the Appendix. Therefore, M_s will also be bounded and there is a guaranteed stability margin for the closed-loop system with MFDOB irrespective of the fundamental frequency.

V. Implementation of MFDOB for $T_c = 0$

In practical electric drives, the computation delay generally exists due to the nonzero calculation time of microcontrollers. To eliminate the computation delay, the PWM command can be updated immediately after sampling the currents. The time sequence is shown in Fig. 9. To avoid switching actions during the control loop calculation, the maximum modulation index is limited depending on the update latency. Hu et al. [21] propose a method for 1-DOF linear controllers to minimize the update latency. It shows that the output voltage is the sum of a historical state and the proportion of the instantaneous current error, which can be expressed by

$$u^k = g_\infty \left(r^k - i^k\right) + u_{ss}^{k-1}. \tag{29}$$

In (29), r and i are the current reference and current feedback, respectively, the superscript indicates the discrete-time index, u_{ss} is a historical state, and the time index $k-1$ means u_{ss}^{k-1} is available before sampling i^k. g_∞ is the direct feed-through gain[1] of the feedback controller. Equation (29) applies to either the stationary or synchronous reference frame. Since r^k and u_{ss}^{k-1} can be prepared before sampling i^k, the simple calculation of (29) enables to minimize the latency from current sampling to the update of PWM command.

[1]The direct feed-through gain g_∞ of a transfer function $C(z)$ is defined such that the remaining part $\bar{C}(z) = C(z) - g_\infty$ is strictly proper.

The method in [21] was intended for 1-DOF controllers by reconstructing the controller architecture to acquire u_{ss}^{k-1}, and the extension for 2-DOF control schemes may be difficult without augmenting redundant states. However, the concept of (29) that u^k is a linear function of i^k can still be utilized. In this manner, the dq-frame output voltage can be expressed as follows:

$$u_{dq}^k = -g_\infty i_{dq}^k + u_{f0}^k. \tag{30}$$

In (30), g_∞ still refers to the direct gain from i_{dq}^k to u_{dq}^k, and u_{f0}^k is the bias when the feedback current is zero. Noting that g_∞ equals the direct feed-through gain of the equivalent feedback controller $K_{fb}(z)$, given by

$$g_\infty = K_p + \hat{b}^{-1}\left(l_0 + \sum_{k=1}^{n} l_{2k-1}\right). \tag{31}$$

With the parameters given in (23), (31) is deduced as follows:

$$g_\infty = K_p + e^{j\omega_e T_s}\frac{\hat{R}_s}{1 - e^{-\hat{R}_s/\hat{L}_s \cdot T_s}}\left(\lambda + \sum_{k=1}^{n} \rho_k c_k\right). \tag{32}$$

The value of u_{f0}^k is not readily available. Based on its definition in (30), it will be obtained as follows. Suppose that the algorithm of the current controller, represented by the gray shadow area in Fig. 6, is realized programmatically with a multi-input–multioutput function controller_run in (33), where x_{dq} represents the controller states to be stored.

$$\left[u_{dq}^k, x_{dq}^k\right] = \text{controller\_run}\left(i_{dq*}^k, i_{dq}^k, \bar{u}_{dq}^{k-1}, x_{dq}^{k-1}\right). \tag{33}$$

As (33) represents the instantiation of the current controller, it will coincide with (30). In this manner, we can acquire u_{f0}^k by invoking this function and virtually setting $i_{dq}^k = 0$

$$\left[u_{f0}^k, \sim\right] = \text{controller\_run}\left(i_{dq*}^k, 0, \bar{u}_{dq}^{k-1}, x_{dq}^{k-1}\right). \tag{34}$$

In (34), the second output is omitted. Equation (34) permits to calculate u_{f0}^k before sampling i_{dq}^k.

The time sequences to implement the MFDOB with reduced digital delay are shown in Fig. 10, and the block diagram is presented in Fig. 11. In Fig. 10, the rotor angle is sampled before current sampling with time $T_{\theta/i}$ and the sampled value

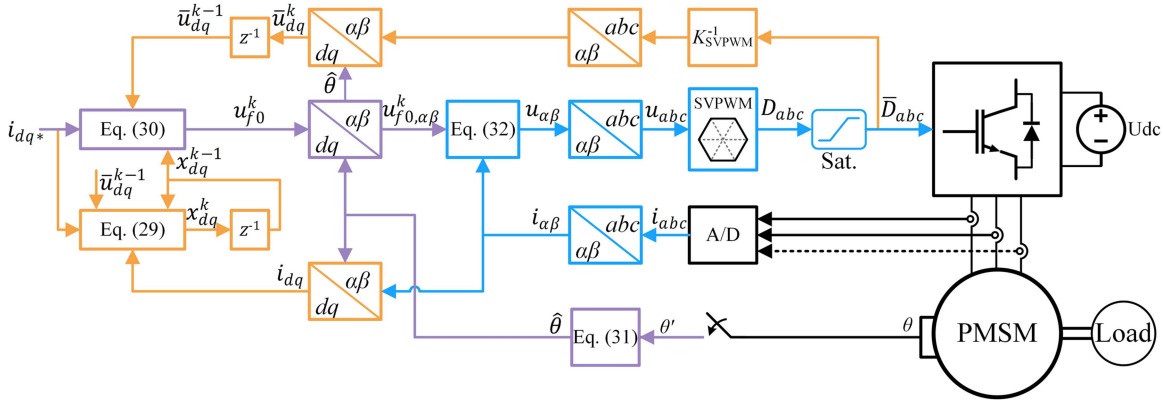

Fig. 11. Implementation of the MFDOB with reduced digital delay. The colors of the signals and blocks are corresponding to the calculation stages in Fig. 10.

is θ'. Then, the rotor angle synchronized to current sampling is predicted by

$$\hat{\theta} = \theta' + \omega_e T_{\theta/i}. \tag{35}$$

To reduce the calculation time for coordinate transformation, (30) is converted to the $\alpha\beta$-frame, yielding

$$u^k_{\alpha\beta} = -g_{\infty,\alpha\beta} i^k_{\alpha\beta} + u^k_{f0,\alpha\beta} \tag{36}$$

where $g_{\infty,\alpha\beta} = e^{j\hat{\theta}}\, g_\infty e^{-j\hat{\theta}}$.

The well-known zero-sequence injection method is utilized for space-vector PWM [29]. The duty cycle of the three-phase PWM command is limited by (37) or (38) depending on the sampling moment [see Fig. 9]

$$T_{\text{update}}/T_s \le \bar{D}_a, \bar{D}_b, \bar{D}_c \le 1, \quad \text{valley sampling} \tag{37}$$

$$0 \le \bar{D}_a, \bar{D}_b, \bar{D}_c \le 1 - T_{\text{update}}/T_s, \quad \text{peak sampling}. \tag{38}$$

After the PWM command is updated, the function controller_run(·) in (33) is invoked again with the measured current to update the controller state x^k_{dq}.

To summarize, the proposed real-time update scheme is divided into three stages.

1) *Precalculation*: Prepare the controller coefficients and trigonometric functions, calculate u^k_{f0} with (34) and transform it to the $\alpha\beta$-frame.
2) *Primary calculation*: After the phase currents are sampled, perform (36), space-vector PWM, and saturation, then update the PWM command.
3) *Postcalculation*: Refresh the controller states with the actual currents using (33) and calculate the saturated dq axes voltage for the next current control period.

This scheme actually transfers the computation load out of the *primary calculation* to reduce the update latency of PWM command. It could also be extended to other 2-DOF controllers.

VI. Experimental Results

The experiments are conducted on a three-phase PMSM connected to a voltage-source inverter with the parameters being pole pairs P_r= 2, phase resistance R_s= 0.29 Ω, inductance L_s= 0.5 mH, PM flux 0.0135 Wb, and dc bus voltage 24 V.

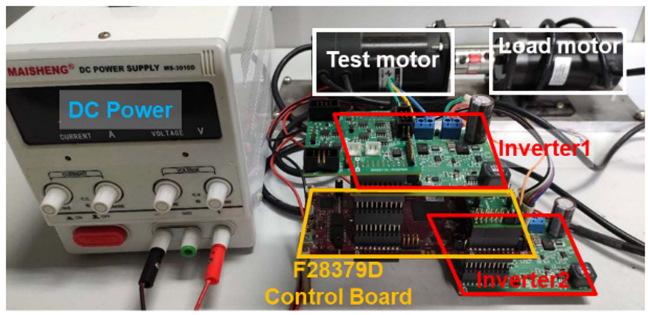

Fig. 12. Schematic diagram of the experimental setup.

The rated current is 5 A and the rated speed is 3000 r/min. The switching and sampling frequency is 10 kHz. Another PMSM is mechanically coupled with the tested motor as a load. A control board with a 200 MHz microcontroller TMS320F28379D is used. The tested motor is operated in the current control mode in the experiments. Fig. 12 presents the experimental setup.

To verify the performance with the proposed MFDOB in mitigating harmonic currents, a large deadtime 3 μs is set to generate harmonic voltage disturbance with the order $6m$ (m = 1, 2, 3, …) in the dq-frame. In addition, an external resistor R_{ex}= 0.4 Ω is added to phase A to emulate an asymmetrical load. Considering $i_d = 0$ and a constant $i_q = I_m$, the voltage drop on the resistor is $v^R_a = R_{\text{ex}}\, I_m \cos\omega_e t$. In the synchronous reference frame, it yields a voltage disturbance

$$v^R_{dq} = \frac{1}{3} R_{\text{ex}} I_m + \frac{1}{3} R_{\text{ex}} I_m e^{-j2\omega_e t} \tag{39}$$

i.e., the combination of a dc component and a harmonic with frequency $2\omega_e$.

The proposed MFDOB with $1T_s$ computation delay and zero computation delay is denoted as MFDOB-1 and MFDOB-0, respectively. Four harmonics with frequencies $2\omega_e, 6\omega_e, 12\omega_e$, and $18\omega_e$ are to be eliminated. The control parameters are $\lambda = 0.3$, ρ_1=ρ_2 =ρ_3 =ρ_4 = 0.01, and K_p= 1 for both controllers. The desired current response is chosen as $R\,(z) = z^{-2}$ for MFDOB-1 and $R\,(z) = z^{-1}$ for MFDOB-0, i.e., deadbeat control. The PI controller [1] and PIR controller [5] are selected for comparative

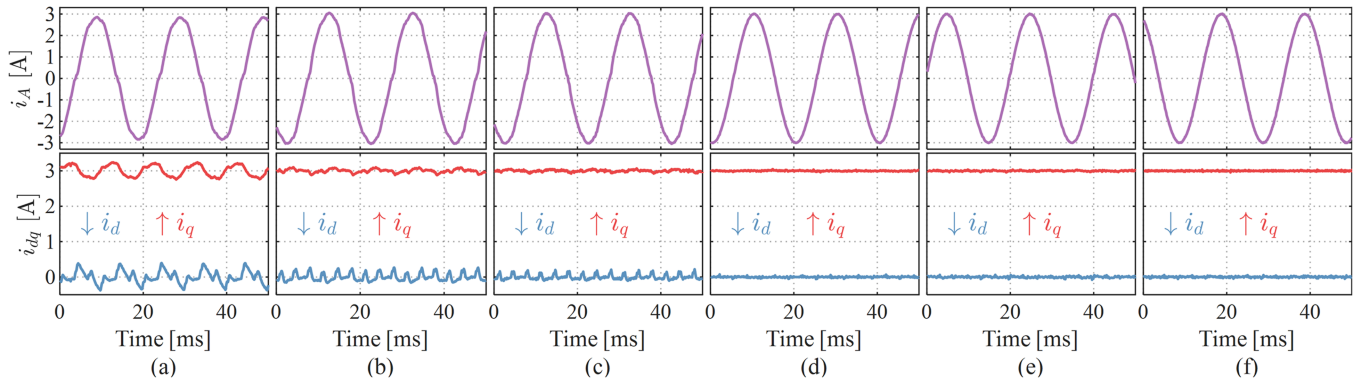

Fig. 13. Steady-state phase A current and *dq* axes' currents at 1500 r/min. (a) PI. (b) PI-DOB (λ_Q=0.5). (c) PI-DOB (λ_Q=1). (d) PIR. (e) MFDOB-1. (f) MFDOB-0.

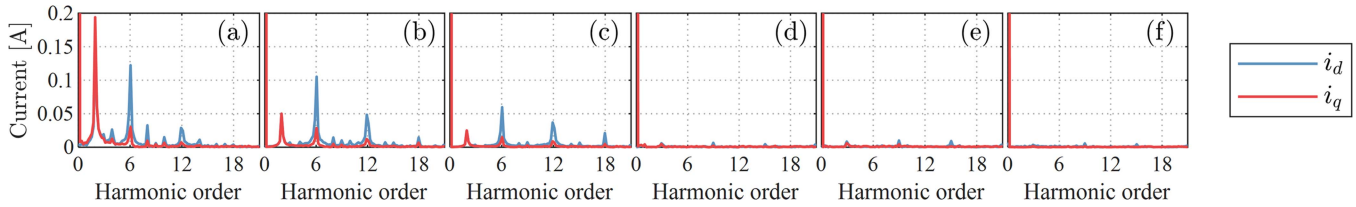

Fig. 14. Harmonic analysis of the *dq* axes' currents in Fig. 13. (a) PI. (b) PI-DOB (λ_Q=0.5). (c) PI-DOB (λ_Q=1). (d) PIR. (e) MFDOB-1. (f) MFDOB-0.

experiments. The gain of the PI controller is $K = 0.3L_s/T_s$. The PI controller [1] incorporating a traditional DOB, denoted as PI-DOB, will also be evaluated, and the Q-filter is selected as $Q(z) = \lambda_Q^2/(z-1+\lambda_Q)^2$. For the PIR controller [5], the resonant frequencies are set as $2\omega_e$, $6\omega_e$, $12\omega_e$, and $18\omega_e$, which are the same as those of the MFDOB. Its control parameters include a gain $K_p = 0.3L_s/T_s$ and a relative gain $k_2 = 0.01$ for all the harmonics.

The steady-state phase current and *dq* axes' currents are shown in Fig. 13 and the harmonic analysis is presented in Fig. 14. In Fig. 13(a), significant current distortion with the PI controller can be observed. In the corresponding harmonic analysis, as shown in Fig. 14(a), the second- and sixth-order harmonic components are dominant in the *dq* axes' currents; other harmonic components except for the 12th order may result from the side effect of the asymmetrical three-phase windings. Fig. 13(b) shows the currents with PI-DOB and λ_Q= 0.5, where the *dq* axes current ripples are smaller than Fig. 13(a). The DOB offers additional attenuation for current harmonics at low frequencies, and the second harmonic component at Fig. 14(b) is reduced significantly. The experimental results of PI-DOB with a higher λ_Q= 1 are presented in Fig. 13(c) and Fig. 14(c). The low-frequency components in Fig. 14(c) are further reduced but not completely eliminated. Since the Q-filter now has been $Q(z) = z^{-2}$, it shows the limited performance of the traditional DOB in rejection harmonic disturbance. In Fig. 13(d), the phase current is more sinusoidal with the PIR controller and the *dq* axes' currents are flatter. The selected harmonic components in Fig. 14(d) are suppressed. The currents with MFDOB-1 in Fig. 13(e) and with MFDOB-0 in Fig. 13(f) are similar to the PIR controller, and the desired harmonics are suppressed in Fig. 14(e) and (f). The latter three controllers exhibit satisfactory steady-state performance.

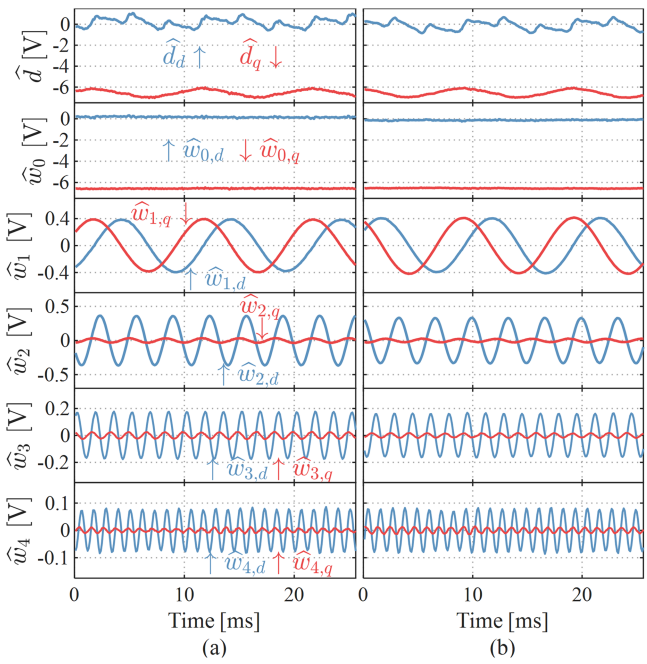

Fig. 15. Estimated disturbance components. (a) MFDOB-1. (b) MFDOB-0.

The disturbance estimation with MFDOB-1 and MFDOB-0 at the same condition as Fig. 13 is shown in Fig. 15(a) and (b), respectively. The two columns are similar as they estimate identical disturbance. The total estimated disturbance is $\hat{d} = \hat{w}_0 + \hat{w}_1 + \hat{w}_2 + \hat{w}_3 + \hat{w}_4$, where $\hat{w}_0$ is the estimation for

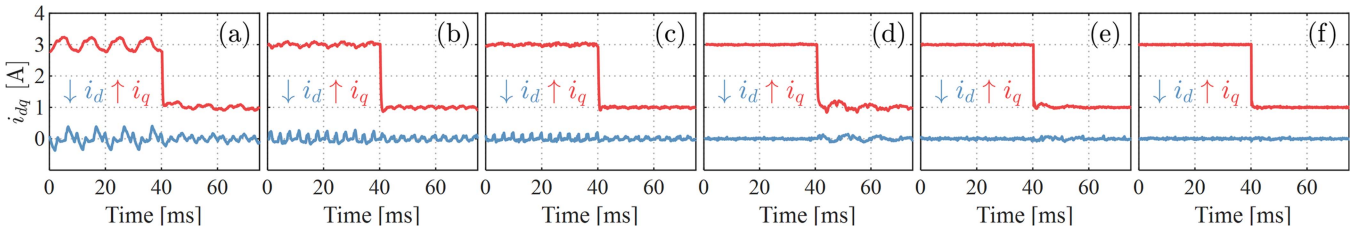

Fig. 16. Current step response at 1500 r/min. (a) PI. (b) PI-DOB (λ_Q=0.5). (c) PI-DOB (λ_Q=1). (d) PIR. (e) MFDOB-1. (f) MFDOB-0.

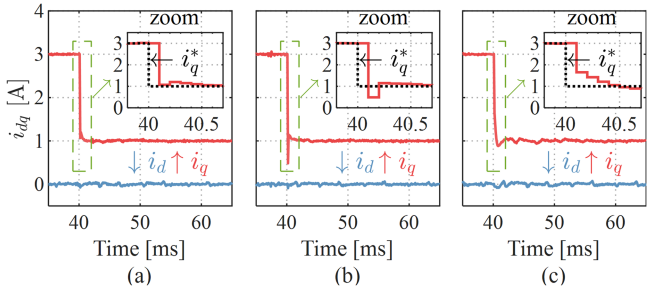

Fig. 17. Current step response with the proposed MFDOB-0 at 1500 r/min under (a) $\hat{L}_s = L_s$, (b) $\hat{L}_s = 1.3L_s$, and (c) $\hat{L}_s = 0.7L_s$.

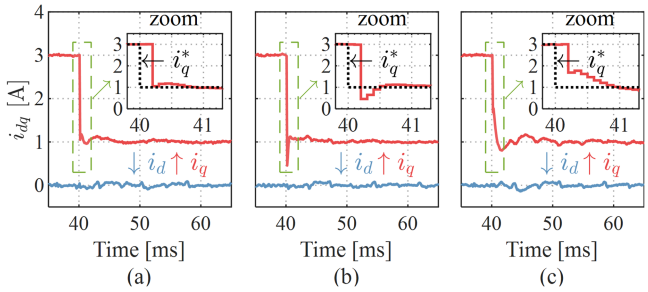

Fig. 18. Current step response with the proposed MFDOB-1 at 1500 r/min under (a) $\hat{L}_s = L_s$, (b) $\hat{L}_s = 1.3L_s$, and (c) $\hat{L}_s = 0.7L_s$.

slow-varying component and $\hat{w}_1, \hat{w}_2, \hat{w}_3$, and $\hat{w}_4$ are the estimated harmonics with frequencies $2\omega_e$, $6\omega_e$, $12\omega_e$, and $18\omega_e$, respectively [see Fig. 2(b)]. Noting that the magnitude of $\hat{w}_1$ is 0.4 V, which matches (39) when $I_m = 3$ A.

The dynamic performance of these controllers is compared through the step response of i_q and shown in Fig. 16. In Fig. 16(a)–(c), the theoretical step responses with the PI and PI-DOB controller are low-pass filter like; however, the uncompensated harmonic components exist under various current magnitudes. Noting that due to the external resistor connected in phase A, the nominal plant differs from the actual one, and the resultant current fluctuations are nearly proportional to the current magnitude. In Fig. 16(d), the resonant modes of the PIR controller are excited in transient states; thus, current oscillations are observed. In Fig. 16(e) with MFDOB-1, the current oscillations also arise but are much smaller compared with Fig. 16(d). The step response with MFDOB-0 in Fig. 16(f) shows the best dynamic performance. That is because the closed-loop system with MFDOB-0 has a wide range of low sensitivities so that the nominal control performance can be preserved.

The current step responses with the MFDOB-0 under different nominal parameter $\hat{L}_s$ are illustrated in Fig. 17. In the zoomed view of Fig. 17(a), the q-axis current lags the reference by one sample, which matches the desired response $R(z) = z^{-1}$. An overestimated $\hat{L}_s$ results in overshoot and an underestimated $\hat{L}_s$ leads to a more damped response, as shown in Fig. 17(b) and (c), respectively. The same tests are also carried out with MFDOB-1 and the results are presented in Fig. 18. It shows that the dynamic performances with both MFDOB-0 and MFDOB-1 are satisfactory under 30% parameter error, while MFDOB-0 is superior in settling time due to the reduced delay.

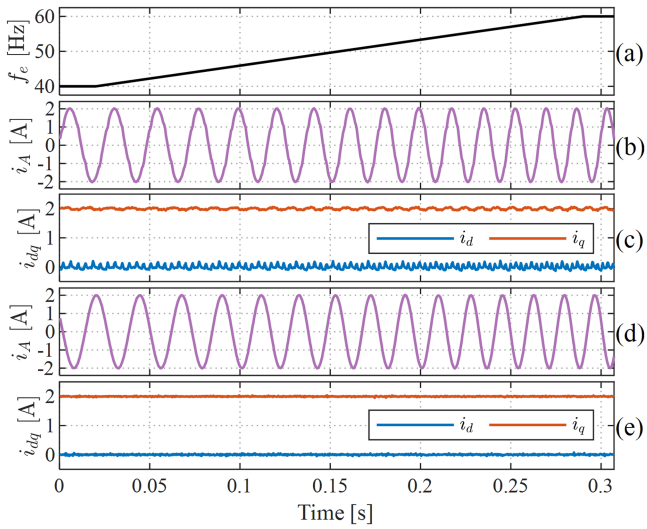

Fig. 19. Current responses with varying f_e from 40 to 60 Hz. (a) Profile of ω_e. (b) Phase A current and (c) dq axes' currents with PI controller. (d) Phase A and (e) dq axes' currents with MFDOB-0.

Fig. 19 shows the current responses at varying fundamental frequencies, where the motor speed ramps up from 1200 to 1800 r/min with the fundamental frequency, as depicted in Fig. 19(a). The phase current and dq axes' currents with a sole PI controller are shown in Fig. 19(b) and (c), respectively, and significant dq axes current ripples can be observed. Fig. 19(d) and (e) show the phase current and dq axes' currents with MFDOB-0, respectively. The dq axes current ripples are eliminated and the phase current is more sinusoidal. Fig. 20 shows the spectral analysis of the d-axis current during the frequency transient state. Due to the varying frequency of the harmonic disturbance, the spectrum with PI controller has two plateaus at $2f_e$ and $6f_e$ range

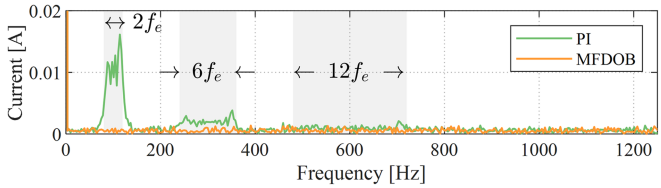

Fig. 20. Spectral analysis of i_d in Fig. 19(c) and (e).

TABLE I
TIME CONSUMPTION OF EACH STAGE OF THE CURRENT LOOP

	T_{AD}	T_{c0}	T_{c1}	T_{c2}
Time(us)	0.3	0.44	3.09	4.56

while they are suppressed with MFDOB-0. The magnitudes around $12f_e$ are not prominent in this test. It not only verifies the ability of MFDOB-0 in rejecting harmonic disturbance but also demonstrates the performance under varying speed/frequency.

The C code of MFDOB-0 is compiled with the C2000 code generation tools v21.6.0.LTS and the optimization level is "-o2." The time consumption of each stage of the current loop is measured with the debug tool in Code Composer Studio and listed in Table I. The update latency T_{update} is 0.74 μs; therefore, the maximum duty cycle under 10 kHz switching frequency will be 98.5%, which is acceptable in real applications.

VII. CONCLUSION

This article proposes the discrete-time frequency-domain MFDOB for multiple harmonic disturbance rejection in variable-speed drives. It features a simple control parameter tuning and a promising stability margin over a wide range of operating frequencies. To lessen the constraints of digital delay on designing DOB, a real-time update scheme with minimized update latency is developed and realizes nearly zero-time computation delay. Superior dynamic performance is achieved due to the reduced delay. Future work will investigate nonlinear DOBs for harmonic disturbance rejection.

APPENDIX

Considering the inner-loop sensitivity $S_i(z) = S_Q(z)$, since the term $|\Phi_k^{ol}(z)/\Phi_k^{cl}(z)|$ is below $(1-\rho_k)^{-1}$ for all frequencies, the envelope curve of $|S_i(z)|$ can be estimated by

$$\bar{S}_Q(z) = \frac{(z-1)D_f(z)}{(z-1+\lambda)^p}\prod_{k=1}^{n}(1-\rho_k)^{-1}. \tag{40}$$

By solving $\mathrm{d}|\bar{S}_Q(e^{j\omega T_s})|/\mathrm{d}\omega = 0$, inner-loop sensitivity peak M_s^i can be estimated by

$$M_{s0}^i \le \max_{\omega}\left|\bar{S}_{Q0}\left(e^{j\omega T_s}\right)\right| = \frac{2}{2-\lambda}\prod_{k=1}^{n}(1-\rho_k)^{-1} \tag{41}$$

$$M_{s1}^i \le \max_{\omega}\left|\bar{S}_{Q1}\left(e^{j\omega T_s}\right)\right| = \frac{2(1+\eta)^2\prod_{k=1}^{n}(1-\rho_k)^{-1}}{\sqrt{(1+2\eta)(3-2\lambda+2(1-\lambda)\eta)}}$$

$$\le \frac{2\left(\lambda+\sum_{k=1}^{n}\rho_k\right)^2\prod_{k=1}^{n}(1-\rho_k)^{-1}}{\lambda\sqrt{\left(\lambda+2\sum_{k=1}^{n}\rho_k\right)\left(3\lambda-2\lambda^2+2(1-\lambda)\sum_{k=1}^{n}\rho_k\right)}} \tag{42}$$

where $\eta = \lambda^{-1}\sum_{k=1}^{n}\rho_k c_k$.

The outer-loop sensitivity peaks can be directly evaluated through $1/(1+K_pP_{dq}(e^{j\omega T_s}))$, giving

$$M_{s0}^o = \frac{a_0+1}{a_0+1-b_0K_p} \tag{43}$$

$$M_{s1}^o = \frac{a_0}{\sqrt{\left(a_0^2+2b_0K_p\sqrt{a_0^2b_0K_p-a_0^2+1}-a_0^2b_0K_p-2b_0K_p\right)}} \tag{44}$$

where $a_0 = e^{-R_s/L_s\cdot T_s}$ and $b_0 = (1-e^{-R_s/L_s\cdot T_s})/R_s$.

REFERENCES

[1] H. Kim, M. W. Degner, J. M. Guerrero, F. Briz, and R. D. Lorenz, "Discrete-time current regulator design for AC machine drives," *IEEE Trans. Ind. Appl.*, vol. 46, no. 4, pp. 1425–1435, Jul./Aug. 2010.
[2] D. G. Holmes, T. A. Lipo, B. P. McGrath, and W. Y. Kong, "Optimized design of stationary frame three phase AC current regulators," *IEEE Trans. Power Electron.*, vol. 24, no. 11, pp. 2417–2426, Nov. 2009.
[3] F. Hans, W. Schumacher, S.-F. Chou, and X. Wang, "Design of multifrequency proportional–resonant current controllers for voltage-source converters," *IEEE Trans. Power Electron.*, vol. 35, no. 12, pp. 13573–13589, Dec. 2020.
[4] M. S. Elkayam and A. Kuperman, "Guidelines for single-parameter multiresonant current controllers design allowing prescribed magnitude tracking of periodic references," *IEEE Trans. Power Electron.*, vol. 36, no. 8, pp. 9536–9546, Aug. 2021.
[5] M. Hu, W. Hua, W. Huang, and J. Meng, "Digital current control of an asymmetrical dual three-phase flux-switching permanent magnet machine," *IEEE Trans. Ind. Electron.*, vol. 67, no. 6, pp. 4281–4291, Jun. 2020.
[6] M. Tian, B. Wang, Y. Yu, Q. Dong, and D. Xu, "Robust adaptive resonant controller for PMSM speed regulation considering uncertain periodic and aperiodic disturbances," *IEEE Trans. Ind. Electron.*, vol. 70, no. 4, pp. 3362–3372, Apr. 2023.
[7] M. Tian, B. Wang, Y. Yu, Q. Dong, and D. Xu, "Discrete-Time repetitive control-based ADRC for current loop disturbances suppression of PMSM drives," *IEEE Trans. Ind. Inform.*, vol. 18, no. 5, pp. 3138–3149, May 2022.
[8] H. Muramatsu and S. Katsura, "An adaptive periodic-disturbance observer for periodic-disturbance suppression," *IEEE Trans. Ind. Inform.*, vol. 14, no. 10, pp. 4446–4456, Oct. 2018.
[9] J. Karttunen, S. Kallio, P. Peltoniemi, and P. Silventoinen, "Current harmonic compensation in dual three-phase PMSMs using a disturbance observer," *IEEE Trans. Ind. Electron.*, vol. 63, no. 1, pp. 583–594, Jan. 2016.
[10] D. Pérez-Estévez, J. Doval-Gandoy, A. G. Yepes, Ó. López, and F. Baneira, "Generalized multifrequency current controller for grid-connected converters with LCL filter," *IEEE Trans. Ind. Appl.*, vol. 54, no. 5, pp. 4537–4553, Sep./Oct. 2018.
[11] Y. Joo, G. Park, J. Back, and H. Shim, "Embedding internal model in disturbance observer with robust stability," *IEEE Trans. Autom. Control*, vol. 61, no. 10, pp. 3128–3133, Oct. 2016.
[12] M. Elkayam, S. Kolesnik, and A. Kuperman, "Guidelines to classical frequency-domain disturbance observer redesign for enhanced rejection of periodic uncertainties and disturbances," *IEEE Trans. Power Electron.*, vol. 34, no. 4, pp. 3986–3995, Apr. 2019.
[13] J. Yang, W.-H. Chen, S. Li, L. Guo, and Y. Yan, "Disturbance/uncertainty estimation and attenuation techniques in PMSM drives—A survey," *IEEE Trans. Ind. Electron.*, vol. 64, no. 4, pp. 3273–3285, Apr. 2017.
[14] M. Hu, W. Hua, Z. Wang, S. Li, P. Wang, and Y. Wang, "Selective periodic disturbance elimination using extended harmonic state observer for smooth speed control in PMSM drives," *IEEE Trans. Power Electron.*, vol. 37, no. 11, pp. 13288–13298, Nov. 2022.
[15] E. Sariyildiz and K. Ohnishi, "A guide to design disturbance observer," *J. Dyn. Syst., Meas., Control*, vol. 136, no. 2, Dec. 2013, Art. no. 021011.

[16] P. F. C. Gonçalves, S. M. A. Cruz, and A. M. S. Mendes, "Disturbance observer based predictive current control of six-phase permanent magnet synchronous machines for the mitigation of steady-state errors and current harmonics," *IEEE Trans. Ind. Electron.*, vol. 69, no. 1, pp. 130–140, Jan. 2022.
[17] E. Sariyildiz and K. Ohnishi, "Design constraints of disturbance observer in the presence of time delay," in *Proc. IEEE Int. Conf. Mechatronics*, 2013, pp. 69–74.
[18] E. Sariyildiz, S. Hangai, T. Uzunovic, T. Nozaki, and K. Ohnishi, "Stability and robustness of the disturbance observer-based motion control systems in discrete-time domain," *IEEE/ASME Trans. Mechatronics*, vol. 26, no. 4, pp. 2139–2150, Aug. 2021.
[19] S. He, D. Zhou, X. Wang, Z. Zhao, and F. Blaabjerg, "A review of multisampling techniques in power electronics applications," *IEEE Trans. Power Electron.*, vol. 37, no. 9, pp. 10514–10533, Sep. 2022.
[20] D. Pan, X. Ruan, C. Bao, W. Li, and X. Wang, "Capacitor-current-feedback active damping with reduced computation delay for improving robustness of LCL-type grid-connected inverter," *IEEE Trans. Power Electron.*, vol. 29, no. 7, pp. 3414–3427, Jul. 2014.
[21] M. Hu et al., "Fast current control without computational delay by minimizing update latency," *IEEE Trans. Power Electron.*, vol. 36, no. 11, pp. 12207–12212, Nov. 2021.
[22] Z. Lin, X. Ruan, H. Zhang, and L. Wu, "A generalized real-time computation method with dual-sampling mode to eliminate the computation delay in digitally controlled inverters," *IEEE Trans. Power Electron.*, vol. 37, no. 5, pp. 5186–5195, May 2022.
[23] A. G. Yepes et al., "Online control strategy for tolerating resistance asymmetry with minimum copper loss in the full torque range for symmetrical six-phase AC drives," *IEEE Trans. Power Electron.*, vol. 38, no. 1, pp. 151–164, Jan. 2023.
[24] A. V. Oppenheim and R. W. Schafer, *Discrete-Time Signal Processing*. London, U.K.: Pearson, 2010.
[25] J. Freudenberg and D. Looze, "A sensitivity tradeoff for plants with time delay," *IEEE Trans. Autom. Control*, vol. 32, no. 2, pp. 99–104, Feb. 1987.
[26] C. A. Busada, S. G. Jorge, and J. A. Solsona, "Comments on 'Digital current control in a rotating reference frame—Part I: System modeling and the discrete time-domain current controller with improved decoupling capabilities'," *IEEE Trans. Power Electron.*, vol. 34, no. 3, pp. 2980–2984, Mar. 2019.
[27] F. M. M. Rahman, V. Pirsto, J. Kukkola, M. Hinkkanen, D. Pérez-Estévez, and J. Doval-Gandoy, "Equivalence of the integrator-based and disturbance-observer-based state-space current controllers for grid converters," *IEEE Trans. Ind. Electron.*, vol. 68, no. 6, pp. 4966–4976, Jun. 2021.
[28] G. Wang, R. Liu, N. Zhao, D. Ding, and D. Xu, "Enhanced linear ADRC strategy for HF pulse voltage signal injection-based sensorless IPMSM drives," *IEEE Trans. Power Electron.*, vol. 34, no. 1, pp. 514–525, Jan. 2019.
[29] A. M. Hava, R. J. Kerkman, and T. A. Lipo, "A high-performance generalized discontinuous PWM algorithm," *IEEE Trans. Ind. Appl.*, vol. 34, no. 5, pp. 1059–1071, Sep./Oct. 1998.

Mingjin Hu (Student Member, IEEE) was born in Jiangxi, China, in 1994. He received the B.Sc. degree in electrical engineering in 2016 from the School of Electrical Engineering, Southeast University, Nanjing, China, where he is currently working toward the Ph.D. degree in electrical engineering.

His current research interests include the discrete-time modeling and advanced control of PMSM drives.

Wei Hua (Senior Member, IEEE) received the B.Sc. and Ph.D. degrees in electrical engineering from Southeast University, Nanjing, China, in 2001 and 2007, respectively.

From 2004 to 2005, he was with the Department of Electronics and Electrical Engineering, The University of Sheffield, U.K., as a Joint-Supervised Ph.D. Student. Since 2007, he has been with Southeast University, where he is currently a Chief Professor and a Distinguished Professor of Jiangsu Province. Since 2010, he has been working with the Yancheng Institute of New Energy Vehicles, Southeast University. He has coauthored more than 180 technical papers. He holds 70 patents in his areas of interest. His teaching and research interests include design, analysis, and control of electrical machines, especially for PM brushless machines and switching reluctance machines, etc.

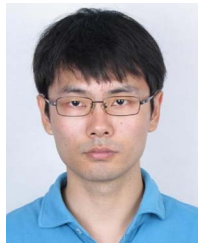

Chenwen Cheng (Member, IEEE) received the B.S. and Ph.D. degrees in electrical engineering from Zhejiang University, Hangzhou, China, in 2012 and 2017, respectively.

From 2018 to 2021, he was a Postdoctoral Researcher with San Diego State University, San Diego, CA, USA. He is currently with Southeast University, Nanjing, China. His research interests include motor control, renewable power generation, and wireless power transfer technologies.

Yuchen Wang was born in Shanxi, China, in 1994. He received the B.Sc. degree in electrical engineering in 2017 from the School of Electrical Engineering, Southeast University, Nanjing, China, where he is currently working toward the Ph.D. degree in electrical engineering.

His current research interests include the analysis and design of embedded magnetic encoder.

Chunyu Lu received the B.Sc. degree in electrical engineering in 2020 from Southeast University, Nanjing, China, where he is currently working toward the M.Sc. degree in electrical engineering with the School of Electrical Engineering.

His main research interests include the parameter design of *LCL* filters and discrete control of high-speed permanent magnet synchronous machines equipped with *LCL* filters.